

Magnetic Ordering in the Frustrated Heisenberg Chain System Cupric Chloride, CuCl_2

M. G. Banks,¹ R. K. Kremer,¹ C. Hoch,¹ A. Simon,¹ B. Ouladdiaf,²
J.-M. Broto,³ H. Rakoto,³ C. Lee,⁴ and M.-H. Whangbo⁴

¹*Max Planck Institut für Festkörperforschung,
Heisenbergstr. 1, D-70569 Stuttgart, Germany*

²*Institut Laue-Langevin, B.P. 156, 38043 Grenoble, France*

³*Laboratoire National des Champs Magnétiques Pulsés - 31432 Toulouse, France*

⁴*Department of Chemistry, North Carolina State University,
Raleigh, North Carolina 27695-8204, U.S.A.*

(Dated: February 12, 2022)

Abstract

We report a detailed examination the magnetic structure of anhydrous cupric chloride CuCl_2 carried out by powder neutron diffraction, magnetic susceptibility and specific heat measurements on polycrystalline and single crystal samples as well as an evaluation of the spin exchange interactions by first principles density functional theory (DFT) calculations. Anhydrous CuCl_2 shows one dimensional antiferromagnetic behavior and long range antiferromagnetic ordering below a Néel temperature of 23.9 K. Neutron powder and single crystal diffraction reveal that, below 23.9 K, CuCl_2 undergoes a phase transition into an incommensurate magnetic structure (propagation vector $(1,0.2257,0.5)$) with a spin-spiral propagating along b and the moments confined in the bc crystallographic plane. Our DFT calculations show that the spin-spiral results from competing ferromagnetic nearest neighbor and antiferromagnetic next-nearest neighbor spin-exchange interaction along the spin chains. Implications for possible multiferroic behavior of CuCl_2 are discussed.

I. INTRODUCTION

Cupric chloride CuCl_2 has a crystal structure in which layers of composition CuCl_2 stack along the c -direction with van der Waals interactions between them. Each CuCl_2 layer consists of CuCl_2 ribbons made up of edge-sharing CuCl_4 square planes such that the axial positions of each CuCl_4 square are capped by the Cl atoms of its adjacent ribbons with long $\text{Cu}\dots\text{Cl}$ distances. Thus, each Cu^{2+} (d^9 , $S = 1/2$) ion is contained in an axially elongated CuCl_6 octahedron, as expected for a Jahn-Teller active Cu^{2+} ion. The magnetic susceptibility measurements exhibit a broad maximum, characteristic of a short-range ordering predicted for low-dimensional magnetic systems.^{1,2,3,4} Historically, CuCl_2 was among the very first magnetic systems whose bulk magnetic properties were analyzed in terms of a linear spin chain model. Heat capacity and NQR measurements indicated a Néel temperature $T_N \sim 23.9$ K for CuCl_2 . To the best of our knowledge the magnetic structure of CuCl_2 has remained unresolved until now.

CuCl_2 is a chemically simple one-dimensional (1D) AFM spin 1/2 quantum chain system. However, by analogy to the CuO_2 ribbon chains found in the magnetic oxides such as LiCuVO_4 and LiCu_2O_2 , the next-nearest-neighbor (NNN) spin exchange coupling along the chain may be essential in addition to the nearest-neighbor (NN) spin exchange in understanding the magnetic properties of CuCl_2 . For these CuO_2 chains, made up of edge-sharing CuO_4 square planes, the NN spin exchange is ferromagnetic (FM), while the NNN spin exchange is strongly AFM, and the resulting geometric spin frustration gives rise to an incommensurate spiral spin ordering and ferroelectric polarization. Similarly, CuCl_2 might undergo a spiral spin ordering within each Cu chain and a long-range Néel ordering as do LiCuVO_4 and LiCu_2O_2 . In the present work we examine the magnetic structure of CuCl_2 in detail by powder neutron diffraction, magnetic susceptibility and specific heat measurements as well as by evaluating its spin exchange interactions on the basis of first principles density functional DFT calculations.

II. EXPERIMENTAL

Single crystals of CuCl_2 were grown in quartz glass ampoules by the Bridgman technique using commercially available powder (Alfa Aesar, ultra dry, purity 99.995%). Special care

was taken in the design of the ampoules to support the elevated vapor pressure of chlorine above the melting point of CuCl_2 . Well-crystallized needle-shape crystals, obtained with the needle axis oriented along the crystallographic b axis were found to be twinned in the ac -plane. Due to the moisture sensitivity of CuCl_2 all handling of the samples was done in an Ar filled glove box. Temperature and field dependent magnetizations ($0 \text{ T} < B_{\text{ext}} < 7 \text{ T}$) were measured using a superconducting quantum interference device magnetometer (MPMS, Quantum Design, 6325 Lusk Boulevard, San Diego, CA.). Magnetizations up to 50 T were measured in pulsed magnetic fields at the Laboratoire National des Champs Magnétiques Pulsés (Toulouse, France) at temperatures of 1.4 and 4.2 K with the field aligned along the crystal b axis. The heat capacities of crystals ($m \sim 20 \text{ mg}$) were measured using a commercial Physical Property Measurements System calorimeter (Quantum Design, 6325 Lusk Boulevard, San Diego, CA.) employing the relaxation method in magnetic fields up to 9 T aligned parallel and perpendicular to the crystal b axis. To thermally anchor the crystals to the heat capacity platform, a minute amount of Apiezon N grease was used. The heat capacity of the platform and the grease was determined in a separate run and subtracted from the total heat capacity. The heat capacity of powder samples ($m \sim 300 \text{ mg}$) was measured in a home-built fully automatic Nernst-type adiabatic calorimeter similar to that described in detail in Refs. 5,6. The powder samples were encapsulated in Duran glass flasks under $\sim 900 \text{ mbar}$ ^4He atmosphere to enable rapid thermal equilibration. The flasks were attached with a minute amount of Apiezon N vacuum grease to the sapphire platform which carries an deposited thin-film stainless steel heater and a calibrated Cernox CX-1050-SD thermometer (Lake Shore Cryotronics, Inc. 575 McCorkle Blvd. Westerville OH 43082). The heat capacities of the sapphire sample platform, the glass flask and the Apiezon vacuum grease were determined in separate runs and subtracted from the total heat capacity. EPR spectra were measured with a Bruker ER040XK microwave X-band spectrometer and a Bruker BE25 magnet equipped with a BH15 field controller calibrated against DPPH. A stepper-motor-controlled goniometer was used to rotate the crystals around an axis perpendicular to the magnetic field plane. The crystals were oriented optically with a precision of $\sim \pm 5^\circ$. 100 kHz field modulation was used to record the first derivative of the signal intensity. The spectra were fitted to a resonance curve with Lorentzian lineshape (zero dispersion) by varying the resonance position as well as the linewidth, intensity and background parameters.

Powder neutron diffraction patterns were collected on the high-intensity two-axis diffrac-

tometer D20 (Institut Laue-Langevin, Grenoble) at a wavelength of 2.4 Å and 1.88 Å in the temperature range $1.8 \text{ K} < T < 50 \text{ K}$.⁷ Single crystal diffraction was carried out on the four-circle diffractometer D10 (Institut Laue-Langevin, Grenoble) at a wavelength of 2.36 Å on a crystal of $\sim 50 \text{ mm}^3$.⁸

III. EXPERIMENTAL RESULTS

A. Crystal Structure

At room temperature, anhydrous cupric chloride CuCl_2 was reported to crystallize with a monoclinic structure (space group $C2/m$) with 2 formula units per unit cell.^{9,10} The crystal structure of CuCl_2 consists of CuCl_2 slabs parallel to the ac -plane that are made up of CuCl_2 chains running along the crystallographic b axis. Such slabs are interconnected along the c axis via van der Waals contacts (cf. Figure 1).

To confirm the crystal structure details of CuCl_2 and to search for structural phase transitions at low temperatures, we collected a series of neutron diffraction patterns on the diffractometer D20 at temperatures $2 \text{ K} < T < 50 \text{ K}$. Patterns with sufficient intensity but improved resolution were collected using neutrons with a wavelength of $\lambda = 1.88 \text{ Å}$ (Ge monochromator) suitable for Rietveld profile refinements. These were done with the FullProf program package¹¹. The patterns were refined assuming the space group $C2/m$ with the Cu atoms in the Wyckoff position (2a) (0,0,0) and the Cl atoms in the position (4i) ($x,0,z$) using a slightly asymmetric pseudo-Voigt profile shape to model the Bragg reflections. Within experimental error the atom coordinates x and z for the Cl atoms are independent of the temperature and amount to $x=0.5065(2)$ and $z=0.2365(3)$. Figure 2 displays the experimental pattern collected at 42.9 K and the results of the Rietveld refinement ($\lambda=1.88 \text{ Å}$). Apart from changes in the lattice parameters, the structure remains unchanged with respect to the room temperature crystal structure of CuCl_2 described by Wells and Burns *et al.*^{9,10} The atom position parameters show no noticeable difference to those of the room temperature structure. The structure parameters at 2.5 and 42.9 K are summarized in Table I.

The temperature dependence of the lattice parameters is displayed in Figure 3. The lattice parameters show a monotonic decrease with temperature. Below $\sim 15 \text{ K}$ they level

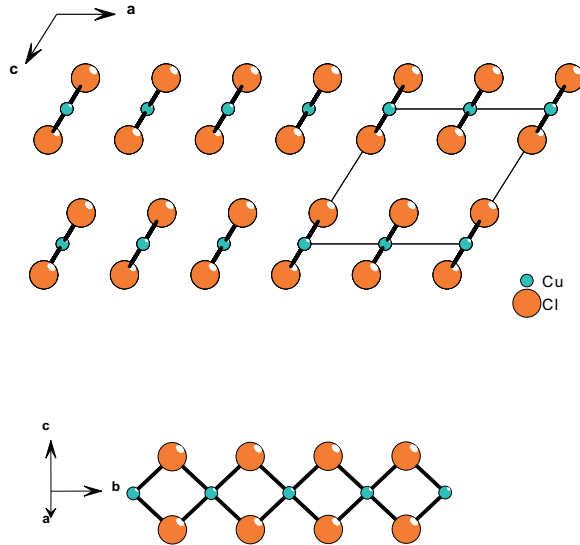


FIG. 1: (Color online) Crystal structure of CuCl_2 projected along $[010]$ drawn using parameters according to Refs. 9,10. A unit cell is outlined by the black solid lines. The Cu atoms are represented by small (blue), and the Cl atoms by large (orange) circles. The lower part of the figure highlights a CuCl_2 ribbons with the b axis along the ribbons. The planes of the ribbons are parallel to the bc plane.

off and remain constant to the lowest temperatures. Near ~ 24 K, especially c and β , exhibit noticeable changes in the slope, which indicate a magnetoelastic response of the lattice to the onset of long-range AFM ordering, as is evidenced by our magnetization and heat capacity experiments discussed in the following paragraphs.

Single-crystal x-ray diffraction on crystals of CuCl_2 were carried out using a laboratory based diffractometer (PDS II, Stoe & Cie., Darmstadt, Germany). These measurements confirmed the crystal structure determined from neutron powder diffraction and showed the crystals to be twinned in the ac - plane. The twinning matrix T relating the Miller indices of the twinned individua was determined to

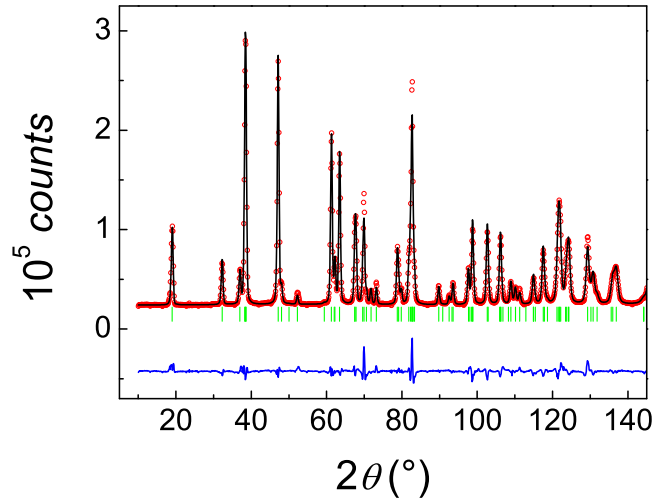


FIG. 2: (Color online) Neutron diffraction pattern (red \circ) ($\lambda=1.888$ Å) of a powder sample of CuCl_2 collected at 42.9 K at the high intensity diffractometer D20 plotted in comparison with the pattern obtained from a profile refinement (solid black line). The difference is shown in the lower part by the (blue) solid line. The positions of the Bragg reflections used to simulate the patterns are indicated by the small (green) vertical bars in the lower part of the figure.

$$T = \begin{pmatrix} 1 & 0 & -1 \\ 0 & -1 & 0 \\ 1 & 0 & 0 \end{pmatrix}. \quad (1)$$

The twinning reverses the b -axis and rotates the axes in the reciprocal space, such that twin-related axes enclose an angle of $180^\circ - \beta \approx 57^\circ$.

IV. MAGNETIC PROPERTIES

A. Magnetic Susceptibility Measurements

Figure 4 displays the magnetic susceptibility of a polycrystalline sample of CuCl_2 . The susceptibility is characterized by a broad maximum centered at ~ 70 K and a Curie-Weiss law (Eq. (5)) behavior at high temperatures (see the detailed discussion of the susceptibility measurement on a crystal below) with a negative Curie-Weiss temperature of ~ -60 K and

| $T(\text{K})$ | $a(\text{\AA})$ | $b(\text{\AA})$ | $c(\text{\AA})$ | $\beta(^{\circ})$ | method |
|---------------|-----------------|-----------------|-----------------|-------------------|-----------------|
| 2.55 | 6.7986(3) | 3.29418(12) | 6.7718(3) | 122.45(2) | neut |
| 42.9 | 6.8010(3) | 3.29437(12) | 6.7768(3) | 122.47(2) | neut |
| 293 | 6.8973(4) | 3.2961(2) | 6.8160(4) | 122.239(3) | x-ray |
| 293 | 6.9038(9) | 3.2995(4) | 6.824(1) | 122.197(8) | x-ray (Ref. 10) |

TABLE I: Lattice parameters of CuCl_2 obtained from neutron powder and x-ray diffraction patterns ($\text{Cu } K\alpha_1$ radiation) at the indicated temperatures. Literature values are given for comparison.

a powder g -factor (see Eq. (5)) of ~ 2.13 .

The negative Curie-Weiss temperature proves predominant AFM exchange interactions, and the broad maximum reveals AFM short range ordering indicative of a low-dimensional magnetic behavior. A kink-like change of the slope near ~ 24 K is due to the onset of long-range AFM ordering. A λ -type anomaly is clearly revealed by the temperature derivative of the quantity $\chi_{\text{mol}} \times T$ ('Fisher's heat capacity', cf. Ref. 12) shown in the inset of Figure 4 from which the Néel temperature T_N is determined to be 23.9(3) K. T_N coincides with the anomalies observed in the temperature-dependence of the lattice parameters (Figure 3). When fitting a Curie-Weiss law to the high temperature data of the powder susceptibility it is found that the fitted parameters (the slope of the reciprocal susceptibility i.e. the effective magnetic moment, and the intercept) are strongly correlated and depend essentially on temperature-independent contributions to the susceptibility (diamagnetic and Van Vleck susceptibilities).

In order to obtain a reliable fit of the magnetic susceptibility of CuCl_2 over a wide temperature range and as well as the temperature independent diamagnetic and paramagnetic corrections to the susceptibility we determined the magnetic susceptibility on a crystal ($B_{\text{ext}}=1\text{T} \parallel b$) up to 600 K. At high temperatures the magnetic susceptibility follows a Curie-Weiss law as demonstrated by the plot of the reciprocal susceptibility in Figure 5.

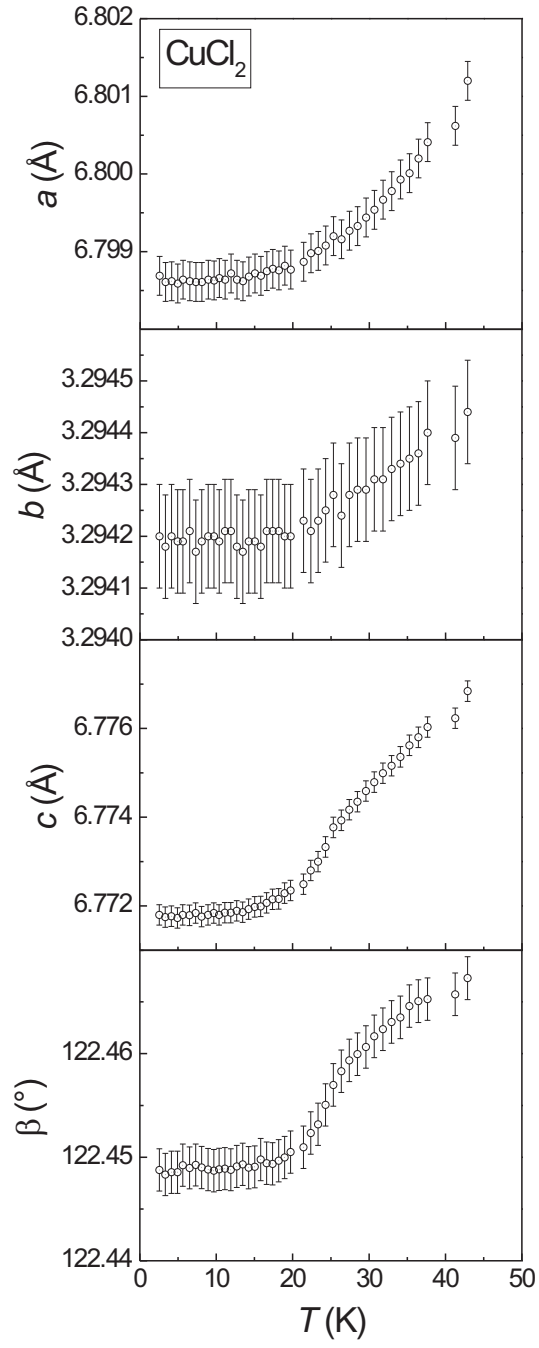
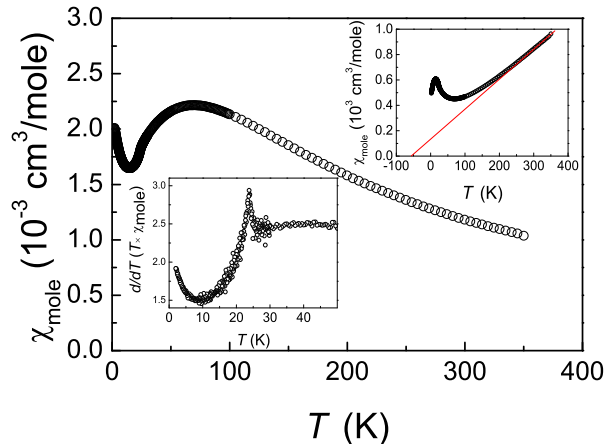


FIG. 3: Temperature dependence of the refined lattice parameters of CuCl_2 resulting from Rietveld profile refinements of the neutron powder diffraction patterns (details see text).



[h]

FIG. 4: (Color online) Temperature dependence of the magnetic susceptibility (not corrected for temperature independent diamagnetic or Van Vleck paramagnetic contributions) of a polycrystalline sample of CuCl_2 determined in an external magnetic field of 1 T. The upper inset shows the reciprocal susceptibility with the (red) solid line indicating a Curie-Weiss law with an intercept on the abscissa at $\sim -60\text{K}$. The lower inset shows $d/dT(\chi_{\text{mol}} \times T)$ ('Fishers heat capacity'). A sharp λ -type anomaly at $23.9(3)$ K indicates the onset of long-range AFM ordering.

Deviations from the Curie-Weiss law are seen already at temperature below ~ 175 K.

At high temperatures, besides the spin susceptibility, $\chi_{\text{spin}}(T)$, temperature independent diamagnetic orbital contributions, χ_{dia} , from the core electronic shells and the Van Vleck paramagnetism, χ_{VV} , from the open shells of the Cu^{2+} ions become important. χ_{dia} can be estimated from the increments using Selwood's tabulated values as $-12 \times 10^{-6} \text{ cm}^3/\text{mole}$ and $-26 \times 10^{-6} \text{ cm}^3/\text{mole}$ for Cu^{2+} and Cl^- , respectively, giving a total temperature independent diamagnetic susceptibility for CuCl_2 of $-64 \times 10^{-6} \text{ cm}^3/\text{mole}$.¹³ An estimate of the Van Vleck contribution, χ_{VV} can be obtained from (cf. Ref 14).

$$\chi_{\text{TIP}} \approx \frac{4N_A\mu_B^2}{\Delta}, \quad (2)$$

where N_A is Avogadro's constant and $\Delta = 10|Dq|$ is the energy separation of the d orbital states in a cubic crystal field, which amounts to approximately $25 \times 10^3 \text{ cm}^{-1}$. With $N_A\mu_B^2/k_B \approx 0.375 \text{ cm}^3 \text{ K}/\text{mole}$ one estimates a Van Vleck susceptibility of Cu^{2+} in a cubic crystal field of the order of $+43 \times 10^{-6} \text{ cm}^3/\text{mole}$. In CuCl_2 due to the Jahn-Teller distortion

the symmetry is reduced and the Van Vleck contribution depends on the actual matrix elements and the energy separation of the orbital states to the $d_{x^2-y^2}$ state. For a detailed discussion see for example Ref. 15. Since these energy splittings are not known at present, we used an alternative method to determine the temperature independent contributions χ_0 : In order to perform this analysis, we assume that the magnetic susceptibility of CuCl_2 can be described by a sum of the temperature dependent spin susceptibility $\chi_{\text{spin}}(T)$ and a temperature independent contribution χ_0

$$\chi(T) = \chi_0 + \chi_{\text{spin}}(T) \quad (3)$$

where χ_0 is composed by the sum of the diamagnetic and the Van Vleck contribution according to

$$\chi_0 = \chi_{\text{dia}} + \chi_{\text{VV}}. \quad (4)$$

At sufficiently high temperatures, $T \gg \theta$, the spin susceptibility $\chi_{\text{spin}}(T)$ can be approximated by a Curie-Weiss law according to

$$\chi_{\text{spin}} \approx \chi_{\text{CW}} = \frac{N_{\text{A}} g^2 \mu_{\text{B}}^2 S(S+1)}{3k_{\text{B}}(T-\theta)}. \quad (5)$$

When fitting the high temperature susceptibility to the sum of equations (4) and (5) it is found that the fitting parameters, g , χ_0 and θ , are strongly correlated, and meaningful results cannot be obtained without fixing one of them. In order to reduce the number of parameters we therefore determined the g-factor, g_b independently by an EPR experiment on a crystal (see below) to $g_b = 2.050(1)$. The EPR experiment also revealed that our CuCl_2 crystals consist of mirror twins in the ab crystallographic plane with the mirror twins having the same b axis. By using $g_b = 2.05$ and fitting Eq. (3) to the (uncorrected) susceptibility data for $T > 150$ (see Figure 5), we determine the following parameters:

$$\chi_0 = -18(1) \times 10^{-6} \text{cm}^3/\text{mole},$$

$$\theta = -71(1)\text{K}.$$

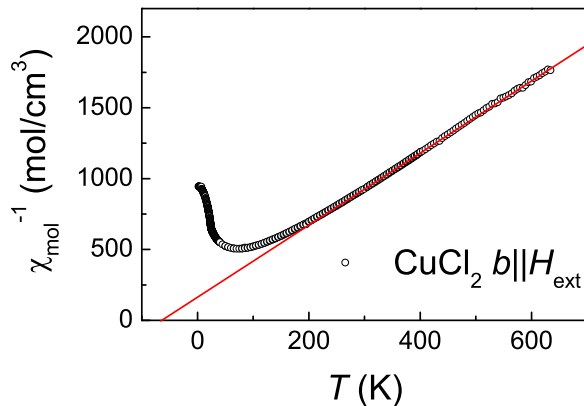


FIG. 5: (Color online) Reciprocal magnetic susceptibility (uncorrected for diamagnetic and Van Vleck contributions) of a crystal of CuCl_2 determined in an external magnetic field of 1 T oriented parallel to the crystallographic b -axis. The (red) solid line represents a Curie-Weiss law including a temperature independent term χ_0 fitted to the data with parameters as given in the text.

B. Magnetization Measurements

Laboratory based magnetization experiments at 1.8 K with $B_{\text{ext}} \parallel b$ evidenced a spin-flop transition near 4 T. Measurements in a pulsed magnetic field at 1.4 K up to ~ 50 T confirmed this result. Evidence for further magnetic phase transitions at fields larger than ~ 4 T could not be found. Figure 6 displays the magnetizations measured in the pulsed field experiment. Saturation is not seen up to 50 T. The 1.4 K magnetization trace shows a slight upward deviation from nonlinearity while the 4.2 K traces within experimental error show a linear dependence of the magnetization over the full field range.

Magnetic susceptibility experiments in various magnetic fields reveal that T_N depends only weakly on the field. The combination of the magnetization and the magnetic susceptibility experiments allows us to construct a magnetic phase diagram for $B_{\text{ext}} \parallel b$ as displayed in Figure 7 with a bicritical point at 5.4(1) T and 24.2(1) K where the paramagnetic, spin flop and Néel phases coexist.

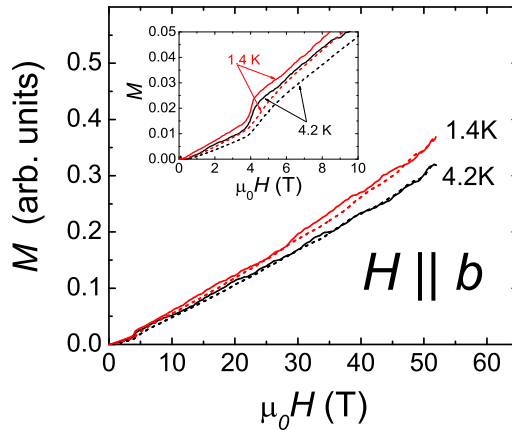


FIG. 6: (Color online) Magnetization of a crystal of CuCl_2 measured at 1.4 K and 4.2 K in a pulsed magnetic field with the magnetic field aligned along b . The inset shows a magnification of the low field data. The solid and dashed lines represent data at 1.4 K and 4.2 K, respectively, measured with increasing (solid line) and with decreasing (dashed line) magnetic field.

C. Electron Paramagnetic Resonance Measurements

In order to determine the g -factors along the principal axes of the g -tensor we carried out EPR measurements on small crystals of CuCl_2 at room temperature at a microwave frequency of 9.46 GHz (X-band) (resonance field ~ 0.33 T). In a monoclinic system, one principal axis of the g -tensor is fixed by symmetry and oriented parallel to the twofold axis, i.e. the crystallographic b axis for CuCl_2 . The remaining two principal axes of the g -tensor lie within the ac plane. To obtain the g -factor along b , a crystal was oriented with the b -axis within the magnetic field plane. Rotation was carried out around an arbitrary axis perpendicular to b . A single resonance line is observed. Figure 8 shows the angular dependence of the g -factor obtained from fits of a field derivative of a Lorentzian to the resonance line. The angular dependence of the g -factor shows the typical oscillating behavior. The minima occur when the field is oriented parallel to the b axis. The g -factor with field oriented parallel to the b -axis amounts to

$$g_b = 2.050(1).$$

The linewidths of the resonance lines exhibit angular dependence and they vary between

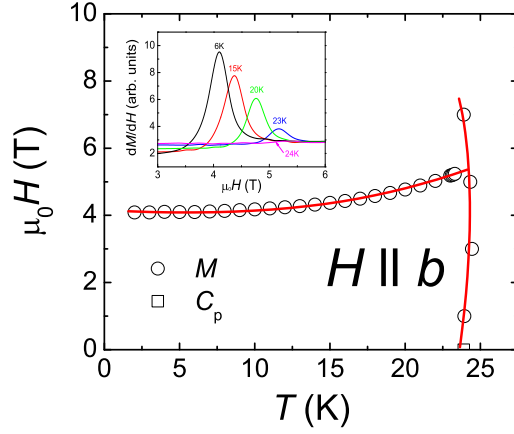


FIG. 7: (Color online) Magnetic phase diagram of CuCl_2 derived from magnetization and heat capacity measurements with the magnetic field aligned along b . The inset displays the derivative dM/dH for selected fields H from which the phase boundaries have been extracted.

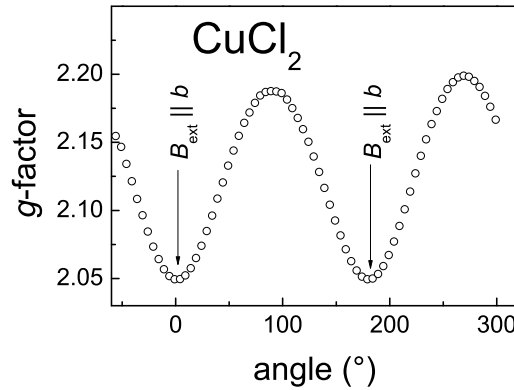


FIG. 8: (Color online) Angular dependence of the g -factor of the EPR resonance line of Cu^{2+} in a crystal of CuCl_2 when the crystallographic b -axis lies within the magnetic field plane. With $b \parallel B_{\text{ext}}$ the g -factor amounts to $2.050(1)$.

20 mT and 40 mT due to small anisotropic exchange components.⁵ Details will be discussed in a forthcoming paper.¹⁷

If the magnetic field was oriented in the ac plane of the crystal (rotation around b -axis), we observed an EPR spectrum that consists of two overlapping resonance lines, indicating that the crystals were twinned. The resonance fields and the linewidths of each line and the

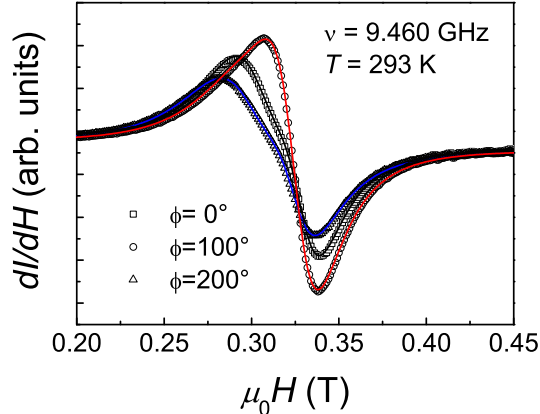


FIG. 9: (Color online) Symbols: EPR spectra of CuCl_2 with the external magnetic field oriented in the crystallographic ac -plane at (arbitrary) angles as given in the inset. The solid lines are fits to the measured spectra assuming two overlapping derivatives of Lorentzian resonance lines with separate resonance fields, linewidths and intensities, respectively.

intensity were obtained by fitting to the spectra the sum of two Lorentzian absorption lines (see Figure 9).

The g -factors of the two lines are shown in Figure 10. One observes the typical oscillating angular dependence of the g -factors on the angle between magnetic field the crystal orientation. Both lines show the same oscillating angular dependence of the g -factor, however with respect to each other shifted by $\approx 57^\circ$. The extremal values are identical within experimental errors. The intensities for the two crystallites are about the same indicating that the investigated twinned crystallites have about the same volume. At angles where both twin-individuals have the same resonance field and g -factors, it is difficult to deconvolute the two resonance line unambiguously. This leads to the rather high error level in the fitted parameters especially at angles where the two g -factor curves intersect.

The principal g -factors, g_1 and g_2 were determined by comparing the results with the general angular dependence of the g -factor for an axial system (Ref. 16)

$$g^2(\phi) = g_1^2 \cos^2(\phi - \phi_0) + g_2^2 \sin^2(\phi - \phi_0), \quad (6)$$

where ϕ is the angle between the external field and the direction of the principal axis 1.

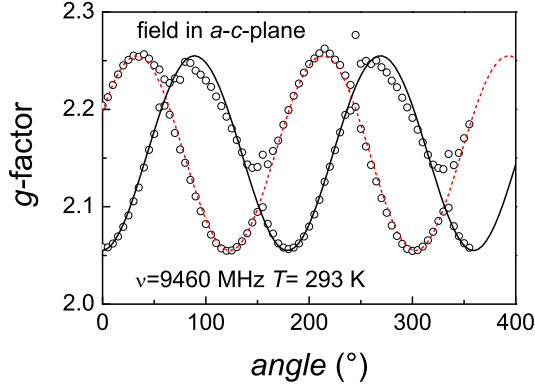


FIG. 10: (Color online) Symbols: EPR spectra of CuCl_2 with the external magnetic field oriented in the crystallographic ac -plane at (arbitrary) angles as given in the inset. The solid lines are fits to the measured spectra assuming two overlapping Lorentzian resonance lines with individual resonance fields, linewidths and intensities each.

ϕ_0 is a phase factor adjusted individually for each individual crystal.

The solid lines in Figure 10 were calculated according to Eq. (6) using

$$g_1 = 2.255(2),$$

$$g_2 = 2.055(2).$$

With $g_b = 2.050(1)$, these values result in an average g -factor of

$$\bar{g} = \sqrt{\frac{1}{3} \sum_i g_i^2} \quad (7)$$

$$\bar{g} = 2.120(5).$$

This value is in good agreement with the g -factor obtained from the powder susceptibility measurement (see. Figure 4).

g_2 and g_b are almost identical indicating that the local symmetry for Cu^{2+} in CuCl_2 is very close to axial with $g_1 \equiv g_{\parallel} = 2.255$ and $g_b \approx g_2 \equiv g_{\perp} \approx 2.05$. Here, we have identified the large g_1 with the g -factor along the quasi-fourfold symmetry axis, perpendicular to the CuCl_4 squares in the ribbons and g_b and g_2 with the g -factors for the magnetic field aligned within the planes of the ribbon.

This finding reflects the local symmetry, which is very close to tetragonal given the elongated CuCl_6 octahedron containing each Cu^{2+} ion. The four Cl atoms in the equatorial plane are all at the same distance of 2.253 Å and the apical Cl atoms at a distance of 2.911 Å ($T = 42.9$ K); the normal of the equatorial plane and the direction to the apical Cl atoms encompass an angle of only 3.2°.

The deviation of the g -factors of the ground state of a $3d^9$ configuration in octahedral field with tetragonal splitting from the g -factor of the free electron is determined by the spin-orbit coupling parameter $\lambda = -\zeta/2S$, where ζ is the one-electron spin-orbit coupling parameter and $S=1/2$. For Cu^{2+} ζ amounts to 829 cm^{-1} (Ref. 16) and the deviations from the free electron g -factor are given by

$$\begin{aligned} g_{\parallel} - 2 &= \frac{8\lambda}{\Delta_0} \\ g_{\perp} - 2 &= \frac{2\lambda}{\Delta_1}, \end{aligned} \tag{8}$$

where Δ_0 and Δ_1 are the energy separations between the $d_{x^2-y^2}$ state and the d_{xy} and the $d_{yz,xz}$ electronic states, respectively.¹⁶ Using our experimental results, Δ_0 and Δ_1 amount to $\sim 26 \times 10^3 \text{ cm}^{-1}$ and $\sim 30 \times 10^3 \text{ cm}^{-1}$, respectively, consistent with the estimate we made from the magnitude of the temperature independent Van Vleck contribution.

The principal axes of the two crystallites are shifted by $180^\circ - \beta \approx 57^\circ$ with respect to each other, where β is the monoclinic angle (cf. Table I). This finding indicates that CuCl_2 crystals generally are twinned with the twins related to each other by a mirror symmetry operation with the mirror symmetry plane in the ac plane making the crystals to appear pseudo-hexagonal. This finding becomes essential for the assignment of the propagation vector of the magnetic structure from elastic neutron diffraction on CuCl_2 crystals.

V. THERMAL PROPERTIES

A. Heat Capacity Measurements

The heat capacity of anhydrous CuCl_2 has been determined before by Stout and Chisholm (Ref. 3) and by Billerey *et al.* (Ref. 18). Figure 11 shows our heat capacities C_p of a CuCl_2

crystal and a powder sample. Our data agree very well with the data published by Stout *et al.* and those of Billerey and collaborators. The data of Stout and Chisholm are shown in Figure 11 for comparison. The heat capacities of our powder sample and the crystal are very similar, and they exhibit λ -shaped anomalies due to the onset of long-range AFM ordering. The anomalies are centered at ~ 23.8 K (crystal: 23.87 K; powder 23.82 K) in good agreement with the values reported by Stout *et al.* (23.91 ± 0.1 K) and Billerey *et al.* (23.9 ± 0.1 K). The maximum value in the λ -anomaly is somewhat larger than the value reported by Stout *et al.* and Billerey *et al.* possibly indicating that our samples structurally are better ordered and contain less structural defects. The λ -anomaly does not change its shape nor shifts the position when a magnetic field of up to 9 T is applied perpendicular to the crystal b axis. Sufficiently below the anomaly where the lattice contribution can be approximated by a Debye- T^3 power law, the total heat capacities follow well the same power law $C_p = C_{\text{ph}} + C_{\text{magnon}} \propto T^3$ indicating magnon contributions from a three-dimensional antiferromagnet.

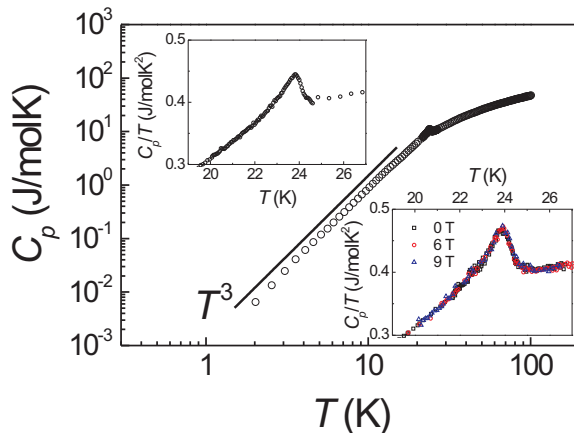


FIG. 11: (Color online) Temperature dependence of the specific heat of CuCl_2 . The main frame shows the heat capacity of a crystal, the lower inset shows the magnetic field dependence of the anomaly at $T_N = 23.85(3)$ K. The magnetic field was directed perpendicular to the b axis. The upper inset displays the heat capacity near T_N of a polycrystalline sample.

The entropy removed by long-range ordering signaled by the anomaly at 23.8 K amounts to $0.60(5)$ J/molK equivalent to 10% of $R \ln 2$ as expected for a $S = \frac{1}{2}$ spin system. The remaining 90% of the entropy apparently are removed by short-range ordering above T_N .

The total heat capacity, C_p , of CuCl_2 contains the spin (magnetic) and contributions from the phonon system (lattice contribution) according to

$$C_p(T) = C_{\text{mag}}(T) + C_{\text{latt}}(T) \quad (9)$$

In order to separate the magnetic contributions, C_{mag} , from the total heat capacity of CuCl_2 , one has to determine the lattice heat contributions, C_{latt} . The lattice contributions can be estimated by fitting a power series expansion to the high temperature regime, where magnetic contributions are negligible, and extending the series to low temperatures. A significantly improved estimate of the lattice heat capacity is usually achieved by measuring the heat capacities of isostructural nonmagnetic compounds. The lattice reference systems appropriate for CuCl_2 would be MgCl_2 and CdCl_2 . Both compounds crystallize with a layered crystal structure similar to that of CuCl_2 .¹⁹ However, the MCl_6 (M=Mg, Cd) octahedra of MgCl_2 and CdCl_2 do not exhibit a Jahn-Teller distortion, and consequently the two-valent anions are coordinated regularly by six Cl atoms at the same distance of 2.64 Å and 2.96 Å for CdCl_2 and MgCl_2 , respectively.¹⁹

Billerey *et al.* determined the heat capacities of MgCl_2 in the temperature range 2 K $< T < 100$ K and constructed the lattice contribution to the heat capacity of CuCl_2 . We re-measured the heat capacities of a polycrystalline sample and of crystalline pieces of high purity (Alfa Aesar 99.99%) MgCl_2 in an extended temperature range. We found that our data for MgCl_2 obtained on two independent samples with two different experimental setups, especially, in the temperature regime relevant for the magnetic part below 100 K deviate markedly from Billerey's data. Our values being up to 10% smaller than Billerey's results.

Additionally we determined the heat capacity of a small polycrystalline beads, typical diameter 2mm) of CdCl_2 (Alfa Aesar 99.998%) The heat capacity of CdCl_2 has been measured before by Itskevich *et al.*(Ref. 20) in a very limited temperature range. Takeda *et al.* (Ref. 21) also determined the heat capacity of CdCl_2 in order to subtract the lattice contribution to the heat capacity of magnetic VCl_2 , but no data are available from the work of Takeda *et al.*. Only the low-temperature cubic term $\propto T^3$ is quoted. Figure 12 shows the heat capacities of MgCl_2 and CdCl_2 as determined in this work in comparison with literature data.

Figure 12 displays the heat capacities of CuCl_2 and of MgCl_2 and CdCl_2 for comparison. As expected, the heat capacity of MgCl_2 is significantly smaller, that of CdCl_2 markedly

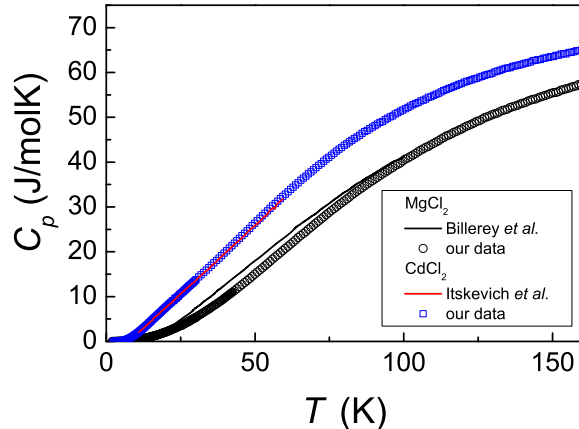


FIG. 12: (Color online) Temperature dependence of the specific heat of a single crystal of MgCl_2 (black \circ) and of CdCl_2 (blue \square) compared with literature data as quoted in the inset (Refs. 18,20).

greater than that of CuCl_2 . A detailed discussion how to construct an adequate lattice reference for CuCl_2 and the magnetic contributions to the heat capacity of CuCl_2 will be given in Section VIII.

VI. NEUTRON DIFFRACTION

A. Elastic Magnetic Scattering of a Powder Sample and a Twinned Crystal

In order to search for magnetic Bragg reflections of the long-range ordered AFM state we examined in detail the low-angular parts of the powder diffraction patterns. A comparison of two diffraction patterns collected in D20's highest intensity mode at a wavelength of $\lambda=2.4$ Å at 2 K and 30K reveals additional magnetic scattering up to $2\Theta \sim 40^\circ$ (Figure 13(a)). Most pronounced is a reflection $\sim 23^\circ$ at the low angle shoulder of the nuclear 001 reflection. Additional, though significantly less intense, magnetic scattering intensity is visible in the 2 K pattern at $\sim 34^\circ$. Both features are not present any more in the pattern collected at 30K and thus can be clearly identified as magnetic Bragg reflections.

Towards low scattering angles, the 30K pattern lies clearly above the 2 K pattern indicating significant paramagnetic scattering in the 30 K pattern. In the difference pattern the magnetic Bragg reflection near 19° is slightly deformed owing to a small shift of the 001

nuclear reflection arising from the contraction of the lattice between 30 K and 2 K.

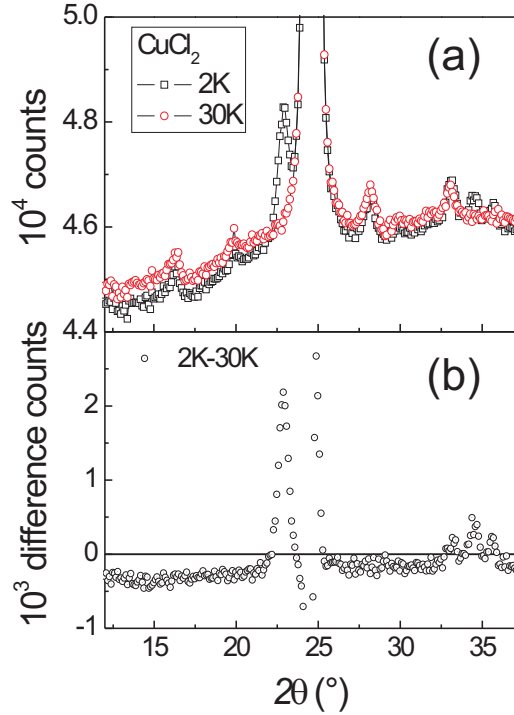


FIG. 13: (Color online) Neighborhood of the 001 nuclear Bragg reflection of CuCl_2 ($\lambda=2.4 \text{ \AA}$) at 2 K and 30K. The additional magnetic Bragg reflection near $2\Theta \approx 23.2^\circ$ is clearly visible. It can be indexed as $-1,0,225,0.5$.

In order to obtain the temperature dependence of this first magnetic Bragg reflection, we collected a series of patterns between 2 K and 45 K in the D20's higher resolution mode using a wavelength of $\lambda=1.888 \text{ \AA}$. The difference between the pattern collected at the respective temperatures and the pattern at 28.9 K was fitted to a Gaussian the intensity of which is displayed versus temperature in Figure 14.

The temperature dependence of the integrated intensities can be well fitted by a critical power law according to Eq. (10) with the critical exponent β

$$I(T) = I_0 (1 - T/T_N)^{2\beta}. \quad (10)$$

A fit of the integrated intensities converges to a Néel temperature $T_N=24.7(1) \text{ K}$ consistent with the magnetic susceptibility and the heat capacity and a critical exponent $\beta=0.16(1)$ (see Figure 14(a)).

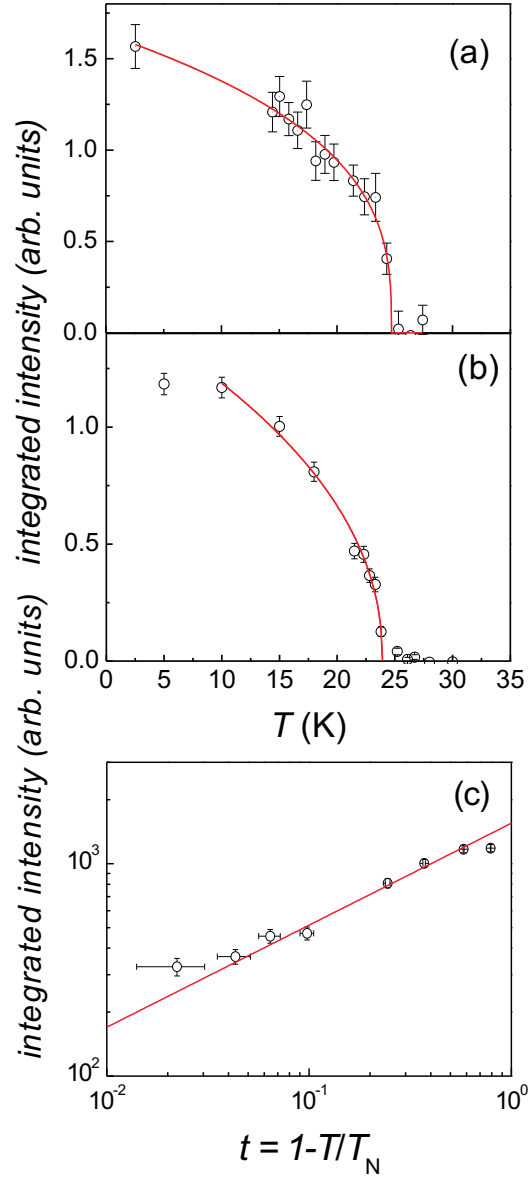


FIG. 14: (Color online) (a) Temperature dependence of the integrated intensity of the magnetic Bragg reflection observed at $2\Theta \approx 18.2^\circ$ ($\lambda=1.888 \text{ \AA}$) (\circ). The solid line is a fit of the experimental data with a power law with a critical temperature $T_N=24.7(1)\text{K}$. (b) Temperature dependence of the integrated intensity of the magnetic Bragg reflection collected on a crystal of CuCl_2 (D10 four-circle diffractometer) $\lambda=2.36 \text{ \AA}$) (\circ). The solid line is a fit of the experimental data with a power law with a critical temperature $T_N=23.9(1)\text{K}$ and a critical exponent $\beta=0.23(2)$. (c) log-log plot of the integrated intensity displayed in (b) vs. the reduced temperature $t=1-T_N/T$. The solid line

Intensities of a set of magnetic Bragg reflections were collected on a twinned crystal. Figure 14(b,c) display the intensity of a strong magnetic reflection collected on a twinned crystal on ILL's four-circle diffractometer D10.^{5,17} Initially, this reflection was indexed as 0 0.776 0.5. In view of the magnetic structure refinement of the powder data (see below) we must conclude that this reflection originates from the related twin individuum in the crystal. Using the inverse of the twin matrix eq. (1) the indexes transform to 0-0.776-0.5 i.e. $1\ 1\ 0 - \vec{\tau}$ and $1\ 1\ 1 - \vec{\tau}$, where $\vec{\tau}$ is the magnetic propagation vector refined from the powder data below. A fit of the integrated intensities of this reflection (solid line in Figure 14(b,c)) gives $T_N=23.9(1)$ and $\beta=0.23(1)$ consistent with the powder diffraction results.

Although the investigated temperature regime is limited, and corrections for critical scattering near T_N have not been applied, the refined critical exponents β obtained from the powder and crystal are significantly lower than those characterizing the well known three-dimensional universality classes (Ising, XY and Heisenberg) for which β ranges between 0.325 and 0.365.²² The refined critical exponent $\beta \sim 0.2$ for CuCl_2 , however, comes close to the predictions of Kawamura for the universality class of of the $\text{SO}(3)$ or the $\text{Z}_2 \times \text{S}_1$ symmetry for systems with chiral order. For such systems β ranges between 0.22 and 0.25.^{23,24,25} Figure 14(c) displays the intensity of a magnetic reflection collected on a twinned crystal on ILL's four-circle diffractometer D10 together with a power law with a critical exponent $\beta = 0.24(2)$

The difference between the 2 K and the 30 K powder diffraction patterns (lower panel of Figure 13) reveals an additional weak triple of magnetic Bragg reflections between 32° and 37° with a peak shape very similar to those of neighboring nuclear reflections. Additionally, the difference patterns allows one to identify magnetic scattering around a scattering angle of $\sim 70^\circ$.

All magnetic Bragg reflections can be indexed with a propagation vector $(1, 0.225, 0.5)$ indicating a doubling of the magnetic cell along the c axis and an incommensurate AFM ordering along b (see Figure 15).

The magnetic structure of CuCl_2 was refined using the D20 2 K and the difference powder diffraction data sets using the program Fullprof. In order to obtain reliable parameters for the nuclear structure (nuclear scale factor, profile parameters), we first refined the 2 K pattern assuming nuclear scattering only. Since magnetic scattering is very small this refinement converges well and provides the lattice and profile parameters and the scale

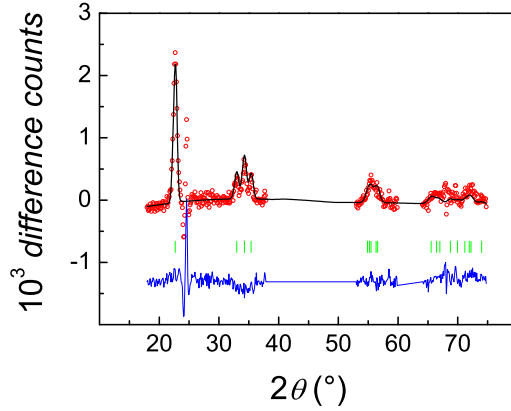


FIG. 15: (Color online) Neutron diffraction pattern (difference of 2 K and 30K patterns) (red \circ) ($\lambda=2.4 \text{ \AA}$) of a powder sample of CuCl_2 collected at the high intensity diffractometer D20 plotted in comparison with the pattern obtained from a profile refinement assuming the magnetic structure described in detail in the text (solid black line). The difference is shown in the lower part by the (blue) solid line. The positions of the the magnetic Bragg reflections used to simulate the patterns are indicated by the small (green) vertical bars in the lower part of the figure.

factor. Subsequently a difference pattern obtained by subtracting the 30 K pattern from the 2 K pattern was used to refine the magnetic structure on the basis of the propagation vector and the nuclear scale factor, which was kept fixed in the refinements. The background of the difference pattern was chosen manually and subtracted. The refinement based on 18 magnetic reflections was successful assuming the nuclear space group $C\bar{1}$ and a helix with the moments confined to the bc plane. Several tests were carried with the moment directions pointing in a more general direction out of the bc plane but did not lead to significantly improved fits.

Assuming this model for the magnetic structure the ordered moment at 2 K converged to

$$\mu(2\text{K}) = 0.50(1)\mu_{\text{B}}.$$

The propagation vector $\vec{\tau}$ at 2 K was refined to

$$\vec{\tau}(2\text{K}) = (1, 0.2257(6), 0.5)$$

implying an angle of $81.2(3)^\circ$ between neighboring moments along the chain. Figure 16 displays the magnetic structure of CuCl_2 at 2 K.

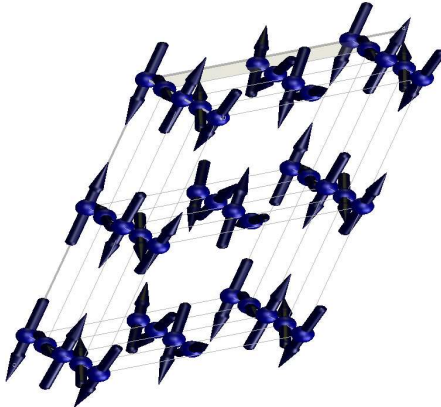


FIG. 16: (Color online) Magnetic structure of CuCl_2 at 2 K. A helix propagating along b with the moments confined to the bc plane. Neighboring moments along b enclose an angle of $\sim 81^\circ$.

VII. DENSITY FUNCTIONAL CHARACTERIZATION OF THE SPIN EXCHANGE INTERACTIONS AND THE SPIN-SPIRAL STATE

To discuss the magnetic structure of CuCl_2 , we consider the intra-chain and the inter-chain spin exchange interactions defined in Figure 17. J_1 and J_2 are the NN and NNN intra-chain spin interactions, respectively. J_3 and J_4 are the inter-chain spin exchange interactions along the c -direction, and J_5 is that along the a -direction. The structural parameters associated with the spin exchange paths $J_1 - J_5$ are summarized in Table II.

To estimate the spin exchange parameters $J_1 - J_5$, we first determine the total energies of the six ordered spin states of CuCl_2 presented in Figure 18 on the basis of first principles density functional theory (DFT) electronic band structure calculations. Our DFT calculations employed the Vienna ab initio simulation package (Ref. 26,27,28) with the projected augmented-wave method, the generalized gradient approximation (GGA) for the exchange and correlation functional, (Ref. 29) the plane-wave cut-off energy of 330 eV, and the sampling of the irreducible Brillouin zone with 36 k -points. To take into consideration of the strong electron correlation associated the Cu 3d state, we performed GGA plus onsite repul-

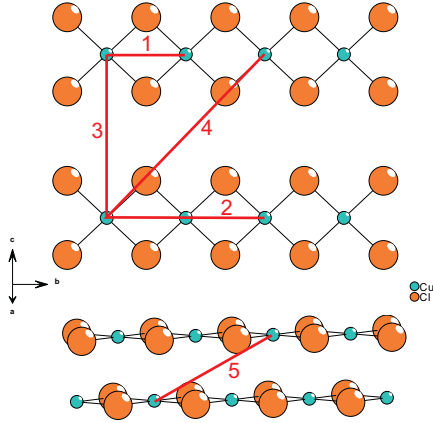


FIG. 17: (Color online) Definition of the five exchange paths $J_1 - J_5$ of CuCl_2 , where the numbers 1 - 5 represent J_1, \dots, J_5 , respectively.

| path | Cu...Cu (\AA) | Cl...Cl (\AA) | \angle Cu-Cl...Cl ($^\circ$) |
|-------|--------------------------|--------------------------|----------------------------------|
| J_1 | 3.299 | - | - |
| J_2 | 6.599 | 3.299 ($\times 2$) | 136.8 |
| J_3 | 6.824 | 3.729 ($\times 2$) | 133.1 |
| J_4 | 9.493 | 4.979 | 174.1 |
| J_5 | 7.608 | 3.808 | 131.7 |

TABLE II: Geometrical parameters associated with the spin exchange paths $J_1 - J_5$ of CuCl_2 .

sion (GGA+U) calculations (Ref. 30) with $U = 3, 5$ and 7 eV on Cu. The relative energies of the six ordered spin states obtained from our GGA+U calculations are summarized in Table III.

The energies of the six ordered spin states can also be written in terms of the spin

| state | $U = 3\text{eV}$ | $U = 5\text{eV}$ | $U = 7\text{ eV}$ |
|-------|------------------|------------------|-------------------|
| FM | 0 | 0 | 0 |
| AFM1 | -11.23 | -8.62 | -6.52 |
| AFM2 | 21.68 | 20.06 | 17.43 |
| AFM3 | 13.77 | 14.09 | 12.95 |
| AFM4 | -31.01 | -22.12 | -15.93 |
| AFM5 | -39.72 | -28.85 | -21.05 |

TABLE III: Relative energies (in meV) of the five ordered spin states of CuCl_2 obtained from the GGA+U calculations.

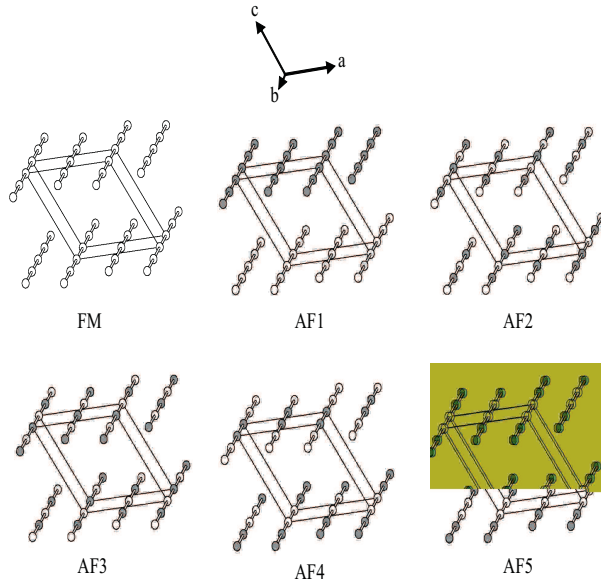


FIG. 18: (Color online) Six ordered spin arrangements of CuCl_2 employed to extract the spin exchange parameters $J_1 - J_5$. The up- and down-spin Cu sites are represented by the open and filled circles, respectively.

Hamiltonian,

$$H = - \sum J_{ij} \vec{S}_i \vec{S}_j, \quad (11)$$

(1) where J_{ij} ($= J_1 - J_5$) is the spin exchange parameter for the spin exchange interaction between the spin sites i and j , while \vec{S}_i and \vec{S}_j are the spin angular momentum operators at the spin sites i and j , respectively. By applying the energy expressions obtained for spin dimers with N unpaired spins per spin site (in the present case, $N = 1$), (Ref. 31,32) the total spin exchange energies per formula unit of the six ordered spin states (see Figure 18) are written as

$$\begin{aligned} E_{FM} &= (-2J_1 - 2J_2 - 2J_3 - 4J_4 - 4J_5) \frac{N^2}{4} \\ E_{AF1} &= (-2J_1 - 2J_2 + 2J_3 + 4J_4 + 4J_5) \frac{N^2}{4} \\ E_{AF2} &= (+2J_1 - 2J_2 - 2J_3 - 4J_4 + 4J_5) \frac{N^2}{4} \\ E_{AF3} &= (+2J_1 - 2J_2 + 2J_3 + 4J_4 - 4J_5) \frac{N^2}{4} \\ E_{AF4} &= (+2J_1 - 2J_3 + 4J_4) \frac{N^2}{4} \\ E_{AF5} &= (+2J_1 + 2J_3 - 4J_4) \frac{N^2}{4} \end{aligned} \quad (12)$$

By mapping the relative energies of the six ordered spin states given in terms of the spin exchange parameters to the corresponding relative energies obtained from the GGA+U calculations, we obtain the values of the spin exchange parameters $J_1 - J_5$ summarized in Table IV.

For all values of U employed, the two strongest spin exchange interactions are the intra-chain interactions J_1 and J_2 . As found for the magnetic oxides with CuO_2 ribbon chains, (Ref. 33,34) J_1 is ferromagnetic while J_2 is antiferromagnetic with J_2 larger in magnitude than J_1 . As a consequence, the intra-chain spin exchange interactions are geometrically frustrated. Except for J_3 , the inter-chain spin exchange interactions are negligible; J_3 is antiferromagnetic and is weaker than J_2 by a factor of approximately four. Because of the intra-chain spin frustration, the magnetic ground state of each CuCl_2 chain is expected to be a spin-spiral state with a certain incommensurate repeat vector q_y along the chain direction,

| state | $U = 3\text{eV}$ | $U = 5\text{eV}$ | $U = 7\text{ eV}$ |
|-------|------------------|------------------|-------------------|
| J_1 | 23.3 | 21.4 | 18.4 |
| J_2 | -41.4 | -31.9 | -24.5 |
| J_3 | -9.1 | -7.0 | -5.3 |
| J_4 | -0.2 | -0.1 | -0.1 |
| J_5 | -0.8 | -0.7 | -0.5 |

TABLE IV: Values of the spin exchange parameters $J_1 - J_5$ (in meV) in CuCl_2 obtained from the GGA+U calculations.

i.e., the b -direction. The inter-chain spin arrangement is expected to be antiferromagnetic along the c -direction due to the spin exchange J_3 . Our calculations of the energy $E(0, q_y, 1/2)$ as a function of the modulation wave vector $\vec{q} = (0, q_y, 1/2)$ shows a minimum at $q_y \approx 0.22$.

The magnetic state with the spin-spiral arrangement removes inversion symmetry and hence should induce ferroelectric polarization. To confirm this prediction, we carried out GGA+U plus spin-orbit coupling (SOC) (Ref. 35) calculations for CuCl_2 that has the commensurate spin-spiral arrangement with $q = (0, 0.25, 0)$ to reduce the computational task. Indeed, our calculations of the ferroelectric polarization using the Berry phase method (Ref. 36,37) for the spin-spiral state of CuCl_2 determined by the GGA+U+SOC calculations lead to nonzero ferroelectric polarizations; with the spin-spiral plane parallel (\parallel) and perpendicular (\perp) to the CuCl_4 ribbon plane, the x -, y - and z - components of the polarizations are calculated to be $P_{\parallel} = (-44.5, 0, 71.6)$ and $P_{\perp} = (5.8, 0, 28.3)$ in units of $\mu\text{C}/\text{m}^2$.

VIII. EXPERIMENT VERSUS THEORETICAL RESULTS

In the following we will compare the implications of the theoretical results for the magnetic susceptibility and the thermal properties. The calculations indicate that the intra-chain exchange is dominant and that the magnetic properties of CuCl_2 have to be described as those of a $S=1/2$ frustrated Heisenberg chain with FM nearest and AFM NN interaction. According to the calculations, the ratio J_1/J_2 is negative and is expected to be of the order of ~ -0.5 to -0.75 . Additionally, there is small but noticeable inter-chain interaction being dominant along the c axis that leads to cooperative AFM ordering and the AFM arrangement along the c direction with the doubling of the magnetic unit cell along c . Magnetic and thermal properties of $S=1/2$ zig-zag Heisenberg chains have been calculated in great detail by exact diagonalization by Heidrich-Meisner and coworkers, and numerical tables are available for a wide range of the ratio $\alpha = J_1/J_2$.^{38,39} These works comprise also the magnetic susceptibility of a $S=1/2$ Heisenberg chain with NN AFM exchange only, i.e., $\alpha=0$ as calculated before by Klümper *et al.* and parametrized by a Padé approximant by Johnston *et al.*^{41,42}

A. Magnetic Susceptibility

Correcting the magnetic susceptibility results with the sum of the temperature independent diamagnetic and Van Vleck corrections to the susceptibility (χ_0) gives the pure spin susceptibility $\chi_{\text{spin}}(T)$ of CuCl_2 . Using the g -factor along b as determined by the EPR measurements, $g_b=2.050(1)$, enables us to compare the magnetic susceptibility of a CuCl_2 crystal measured with magnetic field along the b -axis with model calculations. The only remaining adjustable parameters are the intra-chain exchange constants J_1 and J_2 . The effect of the finite inter-chain exchange J_{inter} on the paramagnetic susceptibilities calculated for the zig-zag chains has been taken into account by employing a mean field approach, which gives as inter-chain interaction corrected susceptibility as(Ref. 40)

$$\chi_{\text{spin}}^{\text{cor}}(T) = \frac{\chi_{\text{spin}}(T)}{1 - (zJ/N_A g_{\perp}^2 \mu_B^2) \chi_{\text{spin}}(T)}. \quad (13)$$

The leading intra-chain exchange J_{\perp} is provided by J_3 (see Table III and Figure 14) and amounts to about 20% of the next-nearest exchange J_2 along the chain. Including intra-

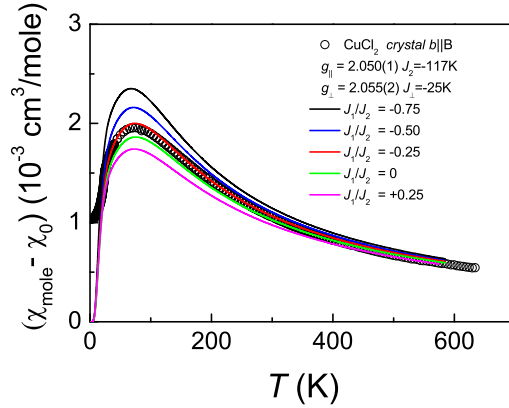


FIG. 19: (Color online) Temperature dependence of the magnetic susceptibility of a crystal of CuCl_2 measured with magnetic field aligned along the crystal b -axis corrected for the sum of diamagnetic and Van Vleck contributions (χ_0) (\circ) compared with the results of exact diagonalization calculations of $S=1/2$ Heisenberg chains with NN and NNN exchange J_1 and J_2 , respectively defining the ratios $\alpha=J_1/J_2$ as given in the inset. The (colored) solid lines were calculated according to Eq. 13 with $\chi_{\text{spin}}(T)$ taken from Ref. 38,39 for $J_2=-117$ K and α s as given in the inset. From top to bottom α amounts to -0.75 , ..., $+0.25$, respectively.

chain exchange according to Eq. 13 renormalizes the calculated susceptibilities by about 8% near the maximum at ~ 73 K. At room temperature the decrease amounts to $\sim 4\%$.

Figure 19 shows the comparison of the spin susceptibility of CuCl_2 as determined in this work with the inter-chain exchange corrected susceptibility of a Heisenberg chain with NN and NNN exchange interaction J_1 and J_2 , respectively.^{38,39}

According to this comparison the magnetic susceptibility of CuCl_2 is best reproduced by an inter-chain exchange corrected susceptibility of a Heisenberg chain with NNN exchange interaction $J_2=-117$ K and a ratio $\alpha \approx -0.25$, i.e., ferromagnetic nearest neighbor exchange as predicted by the DFT calculations. However, the ratio α is markedly smaller than predicted by the DFT calculations (see Table III). Including inter-chain exchange interaction is essential to reproduce the measured susceptibility correctly.

B. Magnetic Heat Capacity

The magnetic contributions to the heat capacity of CuCl_2 has been evaluated before by Stout and Chisholm and subsequently by Billerey and coworkers.^{3,18} Our measurements confirm (see Figure 11(a)) their peak-anomaly at ~ 23 K indicating long-range AFM ordering. Our data agree very well with those of the previous works, and the anomaly is somewhat sharper in our experiment possibly due to the fact that polycrystalline samples have been used before.^{3,18} Stout and Chisholm and Billerey *et al.* used the heat capacities of MnCl_2 and MgCl_2 , respectively, in order to construct an estimate of the lattice heat capacity of CuCl_2 . We redetermined the heat capacities of MgCl_2 and found marked deviations of our data from those of Billerey. We considered also CdCl_2 as another possible system to estimate the phonon contributions to the heat capacity of CuCl_2 and measured the heat capacity of CdCl_2 over a temperature range much wider than covered by the experiments of Itskevich *et al.* (see Figure 12(a)). MgCl_2 and CdCl_2 are diamagnetic and have a crystal structure containing MgCl_2 and CdCl_2 layers, which closely resemble those in the crystal structure of CuCl_2 . However, the MCl_6 (M=Mg, Cd) octahedra are not axially elongated as they are in the CuO_6 octahedra. In addition, owing to the different atomic masses of Cu and Mg, the phonon spectrum of CuCl_2 and MgCl_2 and Cd_2 may be expected to be different, especially at low energies. Although MnCl_2 is magnetic, its AFM ordering occurs at very low temperature, 1.81 K and 1.96 K, and magnetic contributions to its heat capacity are negligible above ~ 10 K.^{44,45} Above 10K, MnCl_2 may therefore provide a reasonable approximation to the lattice heat capacity of CuCl_2 . In order to compensate for the difference in the cation masses, we employed the method of corresponding states and assume that the phonon spectra of MgCl_2 , CdCl_2 and MnCl_2 are very similar to that of CuCl_2 and the different phonon energies can be compensated for by modifying the temperatures.⁴³ Compensation of the different cation mass was done by stretching or compressing the temperature scale by a constant factor. This factor was chosen such that at sufficiently high temperatures where magnetic contributions to the heat capacity vanish the heat capacities of the lattice references match with those of CuCl_2 (see Figure 11). We found factors of 0.88, 0.93 and 1.18 to be appropriate for MgCl_2 , MnCl_2 and CdCl_2 , respectively.

A comparison of the heat capacities of CuCl_2 and MCl_2 (M=Mg, Mn, Cd) reveals significant short-range ordering magnetic contributions to the heat capacity of CuCl_2 up to \sim

100 K, as already concluded by Stout *et al.* and Billerey^{3,18}.

In order to construct a lattice heat capacity reference for CuCl₂ from the heat capacities of MgCl₂, MnCl₂ and CdCl₂, we tried various combinations of the heat capacities of MgCl₂, MnCl₂ and CdCl₂ with temperatures scaled by the factors given above and subtracted these from the total heat capacity of CuCl₂. The resulting magnetic heat capacity of CuCl₂, C_{mag}/T was subsequently integrated and the total magnetic entropy was compared with $R\ln 2$, the entropy expected for a $S=1/2$ magnetic system as a crosscheck.

Due to the very large deviations of the heat capacity of MgCl₂ from that of CuCl₂, especially in the temperature regime below ~ 50 K where magnetic contributions are essential we discarded MgCl₂ and achieved an adequate lattice heat capacity reference by averaging for each temperature the heat capacities of MnCl₂ and CdCl₂.

The magnetic heat capacity of CuCl₂ obtained after subtracting the phonon contributions is shown in Figure 20(b) and (c). In addition to the λ -type anomaly at ~ 23 K the magnetic contributions to the heat capacity are characterized by a broad anomaly due to short-range AFM ordering with maximum at 35 K (in C_{mag}/T and a maximum value of 0.11 J/molK^2). Our data are close to those of Billerey *et al.* but deviate markedly from the data published by Stout *et al.*, who found a significantly higher value for the short-range ordering maximum. The total entropy of the magnetic heat capacity amounts to $0.66(2)R$, very close to $R\ln 2$ expected for the entropy of a spin system with $S=1/2$. Figure 20(c) shows a comparison of the magnetic heat capacity with various model calculations, e.g., the heat capacity of an AFM Heisenberg chain with NN only and with NN and NNN interactions with exchange parameters J_1 and the ratio J_2/J_1 similar to those discussed for the magnetic susceptibility.^{38,42} Both chain models deviate significantly from the experimental data. Surprisingly good agreement of the broad magnetic heat capacity anomaly is obtained for a simple model assuming a spin $S=1/2$ dimer according to

$$H = -J_{\text{dim}}\vec{S}_1\vec{S}_2, \quad (14)$$

with the heat capacity discussed in detail in Ref. 42 for an exchange constant $J_{\text{dim}} \approx -117$ K. The data are also well reproduced by an anisotropic three-dimensional Heisenberg model on a cubic lattice with in-plane exchange J_{\parallel} and interplane coupling J_{\perp} .⁴⁶ With $J_{\parallel} \approx -70$ K and $J_{\perp} \approx 2^{-6}J_{\parallel}$ maximum value and position of the short-range ordering anomaly are rather well reproduced. The onset of three-dimensional ordering showing up as a well separated

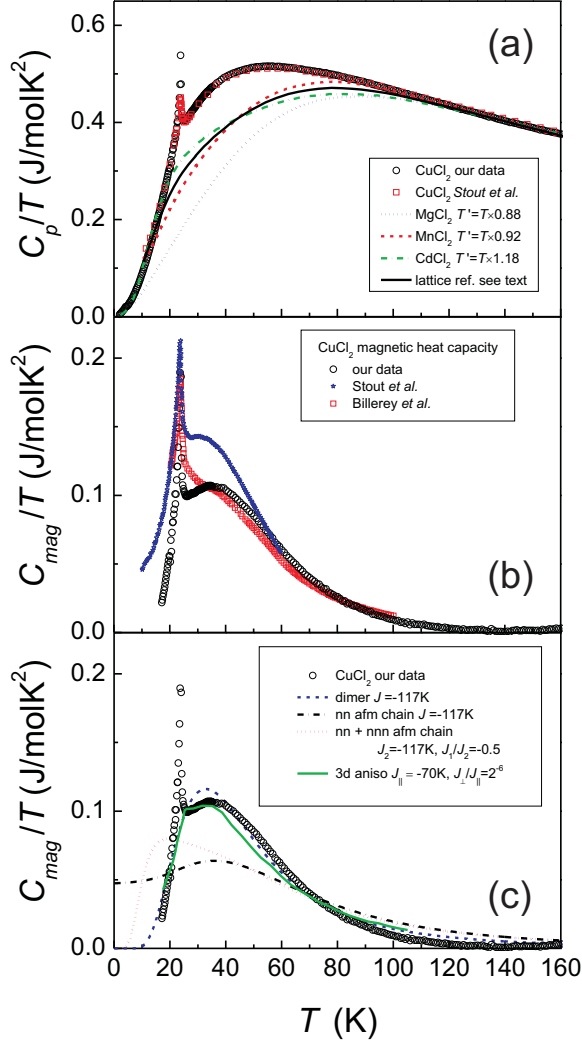


FIG. 20: (Color online) (a) Temperature dependence of the specific heat of a single crystal of CuCl_2 (black \circ) and of a polycrystalline sample measured by Billerey *et al.* (red \square).¹⁸ The heat capacities of MgCl_2 and CdCl_2 as measured in this work and of MnCl_2 (Ref. 44) are also given. Their temperature axes have been rescaled by the factor 0.88, 0.92 and 1.18 for MgCl_2 , MnCl_2 and CdCl_2 , respectively. The (black) solid line is the lattice reference (phonon contribution to the heat capacity) constructed from the heat capacities of MnCl_2 and CdCl_2 as described in detail in the text. (b) Magnetic contribution to the heat capacity of CuCl_2 obtained as the difference of the CuCl_2 data and the lattice reference displayed in (a). Published data by Stout *et al.* and Billerey *et al.* are displayed for comparison. (c) Magnetic heat capacity of CuCl_2 (black \circ) compared with various model calculations as labeled in the inset and discussed in detail in the text.

peak well below the short-range ordering maximum appears close to the cooperative ordering temperature observed for CuCl_2 .

IX. DISCUSSION

Complex compounds containing Cu^{2+} ions with low-dimensional magnetic behavior are legion and have been widely investigated.⁴⁷ However, the detailed magnetic behavior of anhydrous Copper(II)-chloride, CuCl_2 , itself, however, has largely remained a mystery until now. From the early susceptibility studies by deHaas and Gorter and Starr *et al.* it had become evident that CuCl_2 shows unusual AFM properties with a broad maximum in the magnetic susceptibility.^{1,2} The specific heat of CuCl_2 measured by Stout and Chisholm proved long-range AFM ordering at around 23 K and the excess heat capacity extending well above T_N was analyzed in terms of linear chain behavior. Because of a lack of better theoretical foundation this analysis was done using an Ising-type approach.³ A neutron diffraction study in order to determine the long-range ordered groundstate has not been carried out so far.

Our study presents a detailed confirmation of the early susceptibility study carried out on polycrystalline samples and twinned single-crystals of anhydrous CuCl_2 . Susceptibility and heat capacity confirm the one-dimensional AFM properties of CuCl_2 and the Néel temperature 23 K as already found by Stout and Chisholm.³ This rather high Néel temperature as compared to the maximum temperature of the short-range ordering susceptibility maximum occurring at about 70K indicates substantial inter-chain exchange interaction and underlines the conclusion by deJongh and Miedema that CuCl_2 is a rather poor example of a chain structure.⁴⁷

CuCl_2 consists of ribbons of edge-sharing CuCl_4 square planes with Cu^{2+} ions. In such systems a spin helicoidal groundstate can set in along the chain direction at low temperature due to the competition between NN ferromagnetic and NNN antiferromagnetic interactions along the Cu^{2+} chains. The first clear example proven to show such a behavior was LiCuVO_4 that crystallizes with an inverse spinel structure and contains CuO_2 ribbon chains. Helicoidal magnetic ordering with the helix propagating along the chain direction was found by a single-crystal neutron diffraction study.⁴⁸ The frustration scenario with ferromagnetic NN and larger AFM NNN exchange was proven by an inelastic neutron scattering study.⁴⁹

Special interest in the magnetic properties of LiCuVO_4 arose lately from the observation of multiferroic behavior found by Naito *et al.* and Schrettle *et al.*.^{50,51,52} LiCuVO_4 shows a dielectric polarization below the Néel temperature and the polarization can favorably be switched by applying a magnetic field. The origin of this dielectric polarization is due to spin-orbit coupling on the Cu sites, however, the asymmetric charge density distribution necessary for the electric polarization occurs around the O^{2-} ions.³³

LiCu_2O_2 is another Cu^{2+} system with CuO_2 ribbon chains exhibiting helicoidal spin order.^{33,54,55,56,57,58,59} In LiCu_2O_2 , in contrast to LiCuVO_4 , the magnitude of the FM NN (-11 ± 3 meV) exchange is larger than the AFM NNN exchange (7 ± 1 meV). Ferroelectricity in LiCu_2O_2 has been shown by Park and coworkers.⁶⁰

Another related system isostructural with LiCu_2O_2 , which lately has attracted special attention, is NaCu_2O_2 . A helicoidal magnetic ground state has been found by neutron powder diffraction and by NMR experiments.^{61,62,63,64} A review of recent systems with helicoidal ground states has been compiled by Drechsler and collaborators.⁶⁵

All helicoidal systems investigated so far contain oxygen ions to provide superexchange between the Cu^{2+} moments. Clear proof of the helicoidal ground state by magnetic neutron scattering is available only for a few of them. Evidence for systems containing anions other than O^{2+} has not been reported yet.

Anhydrous CuCl_2 is therefore the first example for a halide system for which a helicoidal ground state has been proven unequivocally. Our electronic structure calculations give clear theoretical evidence for a scenario of competing FM NN and AFM NNN exchange interactions. Our experimental results for the bulk magnetic properties and the comparison with their predictions for a $S=1/2$ AFM Heisenberg chain with competing FM NN and AFM NNN exchange support the theoretical predictions. Clear proof for the helicoidal AFM ground state comes from the neutron diffraction work on powder and single crystals. We find a magnetic structure indicating a $S=1/2$ helix in the CuCl_2 ribbon chains. The component of the magnetic propagation vector along the b -axis amounts to $0.2257(6)$ and is in best agreement with the result of the electronic structure calculations. The spin-spiral as refined from diffraction data to is found to lie in the bc plane, consistent with the spin-flop observed in the magnetization data when the magnetic field is oriented along the b axis. The refined magnetic structure indicates a magnetic unit cell which is close to being quadrupled as compared to the nuclear cell with neighboring moments enclosing an angle

of $\sim 81^\circ$ which leads to a significant reduction of NN exchange energy. With respect to the helix this scenario is analogous to that in LiCuV_4 (propagation vector $(0,0.468,0)$ (Ref. 66) and NaCu_2O_2 (propagation vector $(0.5,0.227,0)$).⁶¹

The magnetic susceptibility data indicate the importance of inter-chain interaction, which according to the electronic structure calculation amounts to $\sim 20\%$ - 30% of the intra-chain interaction. Interchain interaction decreases the temperature for the short-range order maximum and provides a better agreement of experimental data and theoretical prediction (Figure 19).

Particularly surprising and striking are the deviations of the short-range ordering contributions to the magnetic heat capacity for CuCl_2 and the heat capacity expected for a $S=1/2$ quantum chain with FM NN and AFM NNN exchange interactions (see Fig. 20(c)). The short-range order contributions match significantly better with a $S=1/2$ dimer singlet-triplet excitation scenario with AFM exchange ~ -117 K corresponding to the exchange found for the NNN interactions along the ribbons. We believe that this coincidence is due to the competing intra-chain competing interactions and the additional AFM inter-chain coupling. The magnetic configuration energy U_{mag} measures the short-range pair correlation function according to (cf. e.g. Ref. 12)

$$U_{\text{mag}} \propto J \langle \vec{S}_0 \vec{S}_1 \rangle, \quad (15)$$

where the subscript 1 denotes a spin adjacent to 0. Thus U_{mag} and the magnetic heat capacity dU_{mag}/dT in a frustrated chain system with coupling to neighboring chains may primarily sense magnetic correlations in a short-ranged cluster in which the configuration energy is determined by the leading AFM exchange to NNN spins.

In summary, anhydrous CuCl_2 shows 1D AFM behavior and long range AFM ordering below a Néel temperature of 23.9 K, below which CuCl_2 adopts an incommensurate magnetic structure $(1,0.2257,0.5)$ with a spin-spiral propagating along b and the moments confined in the bc crystallographic plane. The spin-spiral results from competing FM NN and AFM NNN spin exchange interactions along b . Anhydrous CuCl_2 is the first halide quantum system containing CuCl_2 ribbon chains for which a helicoidal magnetic ground state is realized, and is expected to be ferroelectric below 23.9 K.

Acknowledgments

We thank E. Brücher, S. Höhn, S. Lacher and G. Siegle for experimental assistance. The work at North Carolina State University was supported by the Office of Basic Energy Sciences, Division of Materials Sciences, U. S. Department of Energy, under Grant DE-FG02-86ER45259.

- ¹ W. J. de Haas, C. J. and Gorter, Commun. Leiden 215a (1931).
- ² C. Starr, F. Bitter, A. F. Kaufmann Phys. Rev **58**, 977 (1940).
- ³ J.W. Stout and R.C. Chisholm, J. Chem. Phys. 26, 979 (1962).
- ⁴ C.G. Barraclough and C.F. Ng, Trans. Faraday Soc. 60, 836 (1964).
- ⁵ M. G. Banks, Ph.D. thesis, Loughborough University, Loughborough U.K. (2007).
- ⁶ E. Gmelin, Thermochemica Acta **29**, 1 (1979); E. Gmelin and P. Rödhammer, J. Phys. E (Sci. Instrum.) **14**, 223 (1981); E. Gmelin and K. Ripka, Cryogenics **21**, 117 (1981).
- ⁷ <http://www.ill.eu/d20/home/>
- ⁸ <http://www.ill.eu/d10/>
- ⁹ A.F. Wells, J. Chem. Soc. **1947**, 1670 (1947).
- ¹⁰ P.C. Burns and F.C. Hawthorne, American Mineralogist **78**, 187 (1993).
- ¹¹ J. Rodríguez-Carvajal, Physica (Amsterdam) **192B**, 55 (1993).
- ¹² M. E. Fisher, Philos. Mag. **7**, 1731 (1962).
- ¹³ P. W. Selwood, *Magnetochemistry* 2nd ed. (Interscience, New York, 1956), p. 78.
- ¹⁴ H. Lueken, *Magnetochemie* (Teubner, Leipzig, 1999).
- ¹⁵ M. Takigawa, P. C. Hammel, R. H. Heffner, Z. Fisk, J. L. Smith, and R. B. Schwarz, Phys. Rev. **39**, 300 (1989).
- ¹⁶ A. Abragam and B. Bleaney, *Electron Paramagnetic Resonance of Transition Ions*, (Oxford University Press, 1970).
- ¹⁷ M. B. Banks and R. K. Kremer, unpublished results.
- ¹⁸ D. Billerey, C. Terrier, R. Mainard, and N. Criet, J. Mag. Mater., **30**, 55 (1982).
- ¹⁹ D. E. Partin and M. O'Keeffe, J. Solid State Chem. **95**, 176 (1991).
- ²⁰ E. S. Itskevich and P. G. Strelkov, Soviet Phys. Doklady **1**, 98 (1956).

- ²¹ K. Takeda, K. Ubukoshi, T. Haseda, and K. Hirakawa, *J. Phys. Soc. Jpn.* **53**, 1480 (1984).
- ²² J. C. LeGuillou and J. Zinn-Jusin, *Phys. Rev. Lett.* **39**, 95 (1977).
- ²³ H. Kawamura, *J. Phys. Soc. Jpn.* **54**, 3220 (1985); H. Kawamura, *J. Phys. Soc. Jpn.* **55**, 2095 (1986).
- ²⁴ M. F. Collins, *Magnetic Critical Scattering*, (Oxford University Press 1989).
- ²⁵ B. D. Gaulin, in: *Magnetic Systems with Competing Interactions Ed. H. T. Diep* (World Scientific Publishing Co. 1994).
- ²⁶ G. Kresse, J. Hafner, *Phys. Rev. B* **62**, 558 (1993).
- ²⁷ G. Kresse, J. Furthmüller, *Comput. Mater. Sci.* **6**, 15 (1996).
- ²⁸ G. Kresse, J. Furthmüller, *Phys. Rev. B* **54**, 11169 (1996).
- ²⁹ J. P. Perdew, S. Burke, M. Ernzerhof, *Phys. Rev. Lett.* **77**, 3865 (1996).
- ³⁰ S. L. Dudarev, G. A. Botton, S. Y. Savrasov, C. J. Humphreys, A. P. Sutton, *Phys. Rev. B* **57** 1505 (1998).
- ³¹ D. Dai, M.-H. Whangbo, *J. Chem. Phys.* **114** 2887 (2001).
- ³² D. Dai, M.-H. Whangbo, *J. Chem. Phys.* **118**, 29 (2003).
- ³³ H. J. Xiang and M.-H. Whangbo, *Phys. Rev. Lett.* **99**, 257203 (2007).
- ³⁴ H. J. Xiang, C. Lee and M.-H. Whangbo, *Phys. Rev. B* **76**, 220411(R) (2007).
- ³⁵ K. Kuneš, P. Novák, M. Diviš and P. M. Oppeneer, *Phys. Rev. B* **63**, 205111 (2001).
- ³⁶ R. D. King-Smith and D. Vanderbilt, *Phys. Rev. B* **47**, 1651 (1993).
- ³⁷ R. Resta, *Rev. Mod. Phys.* **66**, 899 (1994).
- ³⁸ F. Heidrich-Meisner, A. Honecker, T. Vekua, *Phys. Rev. B* **74** 020403(R) (2006).
- ³⁹ For detailed numerical tables see <http://www.theorie.physik.uni-goettingen.de/~honecker/j1j2-td/>
- ⁴⁰ R. L. Carlin, *Magnetochemistry*, (Springer Berlin-Verlag 1986).
- ⁴¹ A. Klümper and D. C. Johnston, *Phys. Rev. Lett* **84**, 4701 (2000).
- ⁴² D. C. Johnston, R. K. Kremer, M. Troyer, X. Wang, A. Klümper, S. L. Bud'ko, A. F. Panchula, and P. C. Canfield, *Phys. Rev. B* **61**, 9558 (2000).
- ⁴³ W. O. Boo and J. W. Stout, *J. Phys. E* **10**, 485 (1977).
- ⁴⁴ R. C. Chisholm and J. W. Stout, *J. Chem. Phys.* **36**, 972 (1962).
- ⁴⁵ R. B. Murray, *Phys. Rev.* **100**, 1071 (1955).
- ⁴⁶ P. Sengupta, A. W. Sandvik, and R. R. P. Singh, *Phys. Rev B* **68**, 094423 (2003).
- ⁴⁷ L. J. de Jongh and A. R. Miedema, *Adv. Phys.* **23**, 1 (1974).

- ⁴⁸ B. J. Gibson, R. K. Kremer, A. V. Prokofiev, W. Assmus, and G. J. McIntyre, *Physica B* **350**, e253 (2004).
- ⁴⁹ M. Enderle, C. Mukherjee, B. Fåk, R. K. Kremer, J.-M. Broto, H. Rosner, S.-L. Drechsler, J. Richter, J. Malek, A. Prokofiev, W. Assmus, S. Pujol, J.-L. Raggazzoni, H. Rakoto, M. Rheinstädter, and H. M. Rønnow, *Europhys. Lett.* **70**, 237 (2005).
- ⁵⁰ Y. Naito, K. Sato, Y. Yasui, Y. Kobayashi, and M. Sato, *J. Phys. Soc. Jpn.* **76**, 023708 (2007).
- ⁵¹ F. Schrettle, S. Krohns, P. Lunkenheimer, J. Hemberger, N. Büttgen, H.-A. Krug von Nidda, A. V. Prokofiev, and A. Loidl, *Phys. Rev. B* **77**, 144101 (2008).
- ⁵² Y. Yasui, Y. Naito, K. Sato, T. Moyoshi, M. Sato, and K. Kakurai, *J. Phys. Soc. Jpn.* **77**, 023712 (2008).
- ⁵³ T. Masuda, A. Zheludev, A. Bush, M. Markina, and A. Vasiliev, *Phys. Rev. Lett.* **92**, 177201 (2004).
- ⁵⁴ T. Masuda, A. Zheludev, B. Roessli, A. Bush, M. Markina, and A. Vasiliev, *Phys. Rev. B* **72**, 014405 (2005).
- ⁵⁵ A. A. Gippius, E. N. Morozova, A. S. Moskvin, A. V. Zalesky, A. A. Bush, M. Baenitz, H. Rosner, and S.-L. Drechsler, *Phys. Rev. B* **70**, 020406(R) (2004).
- ⁵⁶ S.-L. Drechsler, J. Málek, J. Richter A. S. Moskvin, *Phys. Rev. Lett.* **94**, 039705 (2005).
- ⁵⁷ M. Papagno, D. Pacilé, G. Caimi, H. Berger, L. Degiorgi, and M. Grioni, *Phys. Rev. B* **73**, 115120 (2006).
- ⁵⁸ L. Mihály, B. Dóra, A. Ványolos, H. Berger, and L. Forró, *Phys. Rev. Lett.* **97**, 067206 (2006).
- ⁵⁹ T. Masuda, A. Zheludev, A. Bush, M. Markina, and A. Vasiliev, *Phys. Rev. Lett.* **92**, 177201 (2004).
- ⁶⁰ S. Park, Y. J. Choi, C. L. Zhang, and S-W. Cheong, *Phys. Rev. Lett.* **98**, 057601 (2007).
- ⁶¹ L. Capogna, M. Mayr, P. Horsch, M. Raichle, R. K. Kremer, M. Sofin, A. Maljuk, M. Jansen, and B. Keimer, *Phys. Rev. B* **71**, 140402(R) (2005).
- ⁶² K.-Y. Choi, V. P. Gnezdilov, P. Lemmens, L. Capogna, M. R. Johnson, M. Sofin, A. Maljuk, M. Jansen, and B. Keimer, *Phys. Rev. B* **73**, 094409 (2006).
- ⁶³ S.-L. Drechsler, J. Richter, A. A. Gippius, A. Vasiliev, A. A. Bush, A. S. Moskvin, J. Mlek, Yu. Prots, W. Schnelle and H. Rosner, *Europhys. Lett.* **73**, 83 (2006).
- ⁶⁴ A. A. Gippius, A. S. Moskvin, and S. L. Drechsler, *Phys. Rev. B* **77**, 180403(R) (2008).
- ⁶⁵ S.-L. Drechsler, J. Richter, R. Kuzian, J. Málek, N. Tristan, B. Büchner, A.S. Moskvin, A.A.

Gippius, A. Vasiliev, O. Volkova, A. Prokofiev, H. Rakotoh, J.-M. Broto, W. Schnelle, M. Schmitt, A. Ormeci, C. Loison, and H. Rosner, *J. Magn. Magn. Mater.* **316**, 306 (2007).

⁶⁶ Note that in LiCuV_4 the nuclear cell contains two Cu atoms along b due to the VO_4 -tetrahedra alternating in their orientation. Accordingly, the propagation vector $(0,0.468,0)$ indicates an approximate doubling of the magnetic cell which again contains four $S=1/2$ entities.